Appl Phys B (2011) 105:883–891
DOI 10.1007/s00340-011-4674-1

Applied Physics B
Lasers and Optics

Near-diffraction-limited dark hollow beam generated by using a hybrid control way

H. Ma · Z. Liu · F. Xi · X. Xu

Received: 12 February 2011 / Revised version: 19 April 2011 / Published online: 30 July 2011

Abstract We propose and demonstrate the generation of dark hollow beam with plane wavefront in the near field based on a hybrid control way by using dual phase only liquid crystal spatial light modulators (LC-SLMs). One phase only LC-SLM redistributes the intensity to the target distribution based on refractive beam shaping system and the other phase only LC-SLM adaptively compensates the wavefront of the output beam by using stochastic parallel gradient descent (SPGD) algorithm. Compared with conventional refractive beam shaping system, the hybrid control way can not only improve the far-field energy concentration of the output beam, but also can correct the phase distortion of the system. Influences of phase distortion on laser beam shaping are analyzed in detail. The theoretical and experimental results show that the near-diffraction-limited dark hollow beam can be successfully generated by using this hybrid control way. The power in the main lobe of the airy disk pattern area in the far field is 2.3 times larger than that without being adaptively compensated.

1 Introduction

In practical applications, the intensity distributions of laser beams are often needed to be redistributed to improve the efficiency. In fields of free space optical communication, deep space optical communication, laser tracking, and nonlinear optics, the dark hollow beam with plane wavefront are required [1–6]. Several methods have been developed to generate dark hollow beams, such as mode conversion, optical holography, hollow-fiber method, transverse-mode selection, nonlinear optical method, 2π phase plate method, and so on [7–15]. Because of their high energy conversion and simple design procedure, the refractive beam shaping systems proposed by Kreuzer for generation of flattop beam have been widely investigated [16–18]. However, the refractive beam shaping system usually contains highly aspheric surfaces. In addition, the refractive beam shaping system is based on the transformation of specific input beam profile to output beam profile, so the systems can only work well for the single input to output conversion [19]. To the best of our knowledge, the experimental generation of dark hollow beam with refractive optical elements has never been reported.

To overcome the shortcomings mentioned above, we reported the experimental generation of annular flattop beam with dual phase only LC-SLMs on the working principle of refractive beam shaping system in Ref. [20]. One phase only LC-SLM redistributes the intensity and the other phase only LC-SLM compensates the wavefront of the output beam. The phase distributions of dual phase only LC-SLMs can be derived from the surface distributions of dual aspheric lenses. However, in practical applications, the compensation of the output beam with the second aspheric lens or phase only LC-SLM may be influenced by many factors such as phase distortions of the input beam and position errors of the shaping systems. The factors mentioned above may greatly reduce the beam quality and far-field energy concentration of the output beam. Adaptive optics is a popular choice for beam controlling and has been used in correction of wavefront aberrations. There are two ways for controlling the deformable mirrors (DMs). One is to measure the wavefront of the input beam exactly by using a wavefront sensor, and the other is to employ some iterative strategies to

H. Ma (✉) · Z. Liu · F. Xi · X. Xu
College of Opto-Electronic Science and Engineering, National University of Defense Technology, Changsha, Hunan 410073, China
e-mail: mahaotong@163.com

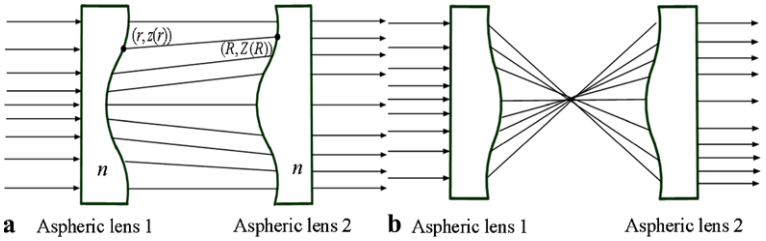

Fig. 1 Configuration of the refractive beam shaping system: (**a**) Galilean system; (**b**) Keplerian system

control the DM. Compared with the first approach, the latter one is easy to implement and can avoid the errors of wavefront measurement [21]. As one kind of diffractive optical elements, phase only LC-SLMs provide an interesting alternative to DMs, because of their high spatial resolution and programmable controller [22]. In this paper, we propose and demonstrate the generation of dark hollow beam with plane wavefront based on the hybrid control way by using dual phase only LC-SLMs. One phase only LC-SLM redistributes the intensity based on the refractive beam shaping system and the other adaptively compensates the wavefront of the output beam by using SPGD algorithm (employing the iterative strategy). The technique combines the advantages of refractive beam shaping system and adaptive optics. Compared with the conventional refractive beam shaping system, the far-field energy concentration of the output beam can be greatly improved and the phase distortion of the system can be effectively corrected.

This paper is organized as follows. In Sect. 2, the working principle is introduced. Some comparisons between the dark hollow beam generated by the conventional refractive beam shaping system and the hybrid control way are numerically calculated. Section 3 reports the experimental results of transformation of quasi-Gaussian beam into near-diffraction-limited dark hollow beam by using the hybrid control way. In Sect. 4, the conclusions are given.

2 Working principle and numerical simulation

In this paper, the intensity redistribution is based on the refractive beam shaping system and the wavefront compensation is based on the adaptive optics (employing the iterative strategy). Figure 1 shows an overview of the basic optical configurations of refractive beam shaping system [20]. The working principle is that the first aspheric lens redistributes intensity of the input beam to desired distribution at the second aspheric lens plane and the second aspheric lens re-collimates the output beam. For each case, a ray parallel to optical axis enters the first aspheric lens at arbitrary radial position r, emerges from the second aspheric lens at radial position R. The terms $z(r)$ and $Z(R)$ represent the first and second surface profiles, respectively. The refractive beam shaping system must meet two requirements: energy conservation and equal optical path.

Based on the energy conservation, the relationship between input and output beam can be given by

$$\int_0^r P_{\text{input}}(x)x\,dx = \int_0^R P_{\text{output}}(x)x\,dx. \tag{1}$$

The relationship between r and R for given input and output intensity distributions can be numerically derived from (1), which is shown in (2):

$$R = h(r). \tag{2}$$

According to the treatment of Kreuzer [18], the surface distributions of dual aspheric lenses in Galilean beam shaping system can be given by

$$z(r) = \int_0^r \left\{(n^2-1) + \left[\frac{(n-1)d}{h(x)-x}\right]^2\right\}^{-1/2} dx, \tag{3}$$

and

$$Z(R) = \int_0^R \left\{(n^2-1) + \left[\frac{(n-1)d}{h^{-1}(x)-x}\right]^2\right\}^{-1/2} dx. \tag{4}$$

The surface distributions of dual aspheric lenses can be translated into phase distributions based on the Fourier Optics. The phase distributions of Galilean beam shaping system can be given by [20]

$$\phi_{\text{phase1}}(r) = \frac{2\pi[z_{\text{edge}} - z(r) + nz(r)]}{\lambda}, \tag{5}$$

and

$$\phi_{\text{phase2}}(R) = \frac{2\pi[nZ_{\text{edge}} - nZ(R) + Z(R)]}{\lambda}, \tag{6}$$

where $z(r)$ and $Z(R)$ denote the sags of the first and second aspheric lenses, respectively; z_{edge} and Z_{edge} denote the edge sags of the first and second aspheric lenses; λ represents the wavelength and n represents refractive index of the shaping system. Loading the phase distributions onto the input beam with phase only LC-SLMs, desired intensity distribution with plane wavefront can be realized. However, in practical applications, re-collimation of the output beam by the second aspheric lens may be influenced by many factors, which include wavefront distortion of the input beam and

position errors of the shaping system. To overcome these shortcomings, we propose the adaptive compensation of the output beam based on the SPGD algorithm. The working principle is shown in Fig. 2. In Fig. 2, the aspheric lens redistributes the intensity to target distribution on the adaptive compensation system plane and adaptive compensation system compensates the wavefront of the output beam. Working principle of the adaptive compensation system is given in Sect. 2.2.

2.1 Influences of wavefront distortions on refractive beam shaping system

The refractive beam shaping system is based on awareness of input and output beam profiles. The input beam with no wavefront distortion is assumed in the design procedure. The refractive beam shaping system may be influenced by many factors, including phase distortion, optical alignment errors, etc. It is very important to study the shaping effect and influences of wavefront distortions in practical applications. In the present paper, only the beam with low-order phase aberrations (tilt and defocus) is considered. However, the technique can also be used in correction of alignment errors and other phase aberrations.

In simulation, the intensity distributions of input and output beam are chosen as Gaussian and dark hollow Gaussian profiles, and are given by

$$P_{\text{input}}(r) = \exp\left(-\frac{2r^2}{w_o^2}\right) \tag{7}$$

and

$$P_{\text{output}}(r) = \left(\frac{r^2}{w^2}\right)^p \exp\left(-\frac{r^2}{w^2}\right), \tag{8}$$

where w_o and w are the beam waists of Gaussian and dark hollow Gaussian beams, p is the order of dark hollow Gaussian beam. The Gaussian beam with $w_o = 3$ mm and the dark hollow beam with $w = 1$ mm, and $p = 3$ are chosen as the input and output beam profiles. The refractive index and distance between two aspheric lenses are $n = 1.45$ and $d = 400$ mm. The surface and phase distributions of aspheric lenses can be numerically derived by varying the radial position. According to the Kirchhoff diffraction theory, we calculate the intensity and phase distributions of the beam after passing through the aspheric lenses beam shaping system and the results are shown in Fig. 3(a) and (b).

From Fig. 3(a), (b) and (c), it can be found that the dark hollow beam with nearly plane wavefront is realized. To study the far-field intensity distributions, the lens with focal length 5.5 m is used to focus the output beam. The far-field intensity distribution, which exhibits airy disk pattern, is shown in Fig. 3(c). Figure 4(a), (b) and (c), shows the Gaussian beam with defocus aberration ($f = 6m$) passing through the refractive beam shaping system. It can be found that the dark hollow intensity distribution is realized in the near field, but the energy concentration in the far field degrades. Figure 5(a), (b) and (c), shows the Gaussian beam with tilt aberration ($t_x = 0.5$ mrad) passing through the refractive beam shaping system. As we know, the influence of the input beam with tilt wavefront aberration is the same as the shaping system with tilt alignment error. The simulation

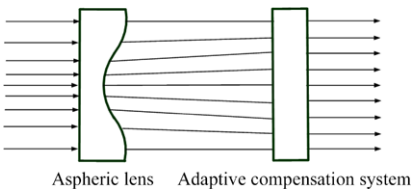

Fig. 2 Configuration of the beam shaping system by using the hybrid control way

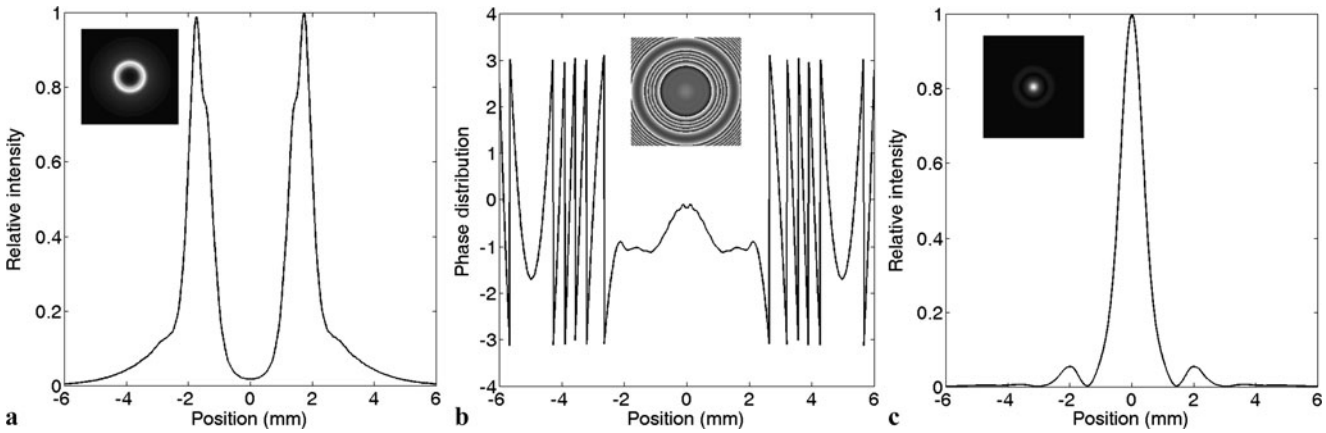

Fig. 3 Intensity and phase distributions of the beam after passing through the aspheric lenses beam shaping system: (**a**) intensity distribution, (**b**) phase distribution, (**c**) far-field intensity distribution

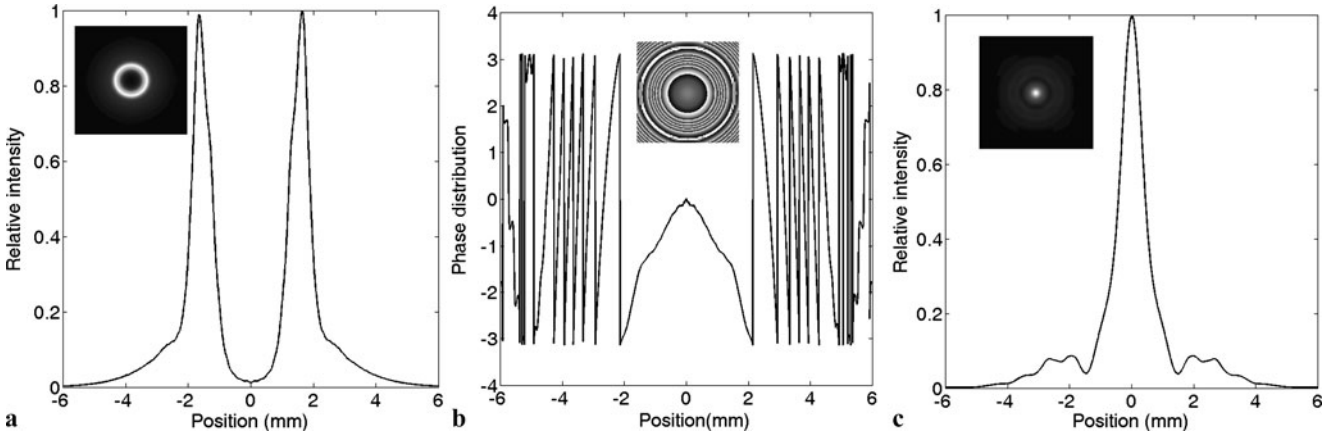

Fig. 4 Intensity and phase distributions of the beam with defocus aberration ($f = 6$ m) passing through the aspheric lenses beam shaping system: (**a**) intensity distribution, (**b**) phase distribution, (**c**) far-field intensity distribution

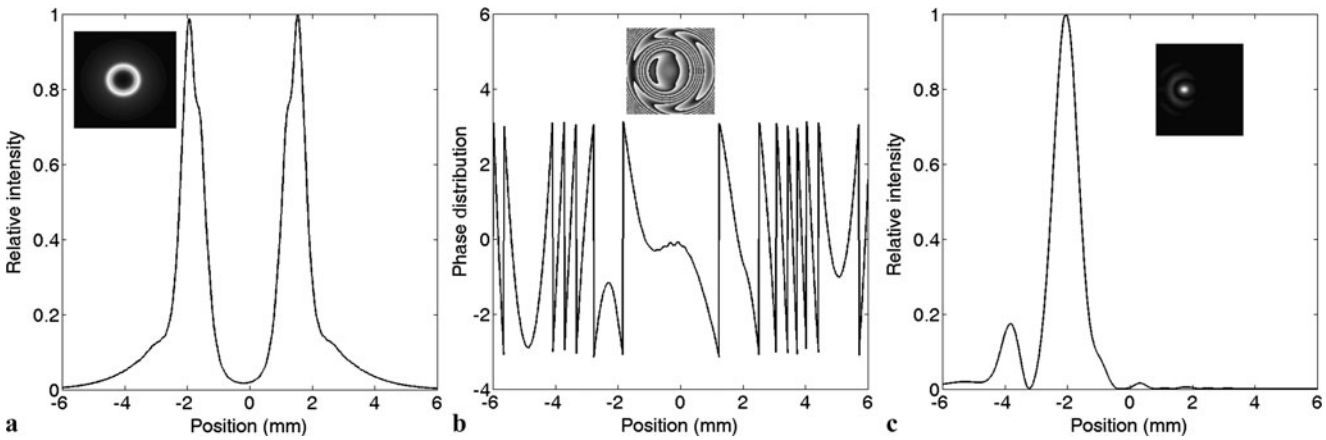

Fig. 5 Intensity and phase distributions of the beam with tilt aberration ($t_x = 0.5$ mrad) passing through the aspheric lenses shaping system: (**a**) intensity distribution, (**b**) phase distribution, (**c**) far-field intensity distribution

results show that the dark hollow intensity distribution can also be realized in the near field, but the centroid of dark hollow beam moves to one side and the corresponding far-field energy concentration degrades.

Based on Figs. 3, 4, and 5, it can be found that the conversion of quasi-Gaussian beam with small wavefront distortion to dark hollow beam in the near field can be realized, but the corresponding far-field energy concentration degrades greatly because of its wavefront distortions. The refractive beam shaping system can do nothing to the dynamic phase distortion of the input beam. The influence of small phase aberration on the near-field intensity distribution is much smaller than that on the far-field intensity distribution. To overcome the shortcoming of refractive beam shaping system, we propose the adaptive compensation of the output beam based on the SPGD algorithm by using the iterative strategy. In the next section, the adaptive compensation results based the SPGD algorithm corresponding to Figs. 3, 4 and 5 are calculated and discussed.

2.2 Adaptive compensation of the output beam

The SPGD algorithm, which is well suited for finding a global minimum or maximum of some objective error functions by optimizing many variables, has been used in astronomy and coherent beam combination [23, 24]. According to the analysis of Vorontsov, for high spatial resolution phase corrector, the maximum convergence speed can be achieved if the Zernike polynomials are chosen as a set of influence functions, which is regarded as the modal control strategy in Ref. [23]. The phase distribution which would be loaded on phase only LC-SLM can be represented as

$$\varphi_{\text{phase2}}(r,\theta) = \sum_{i=2}^{n} a_i Z_i(r,\theta), \tag{9}$$

where $Z_i(r,\theta)$ is the ith order Zernike polynomial, a_i is the Zernike expansion coefficient, which is also the control signal. The quality metric $J = J(\boldsymbol{a})$ is a function of the control parameters $\boldsymbol{a} = \{a_2, \ldots, a_n\}$. The definition of $J = J(\boldsymbol{a})$

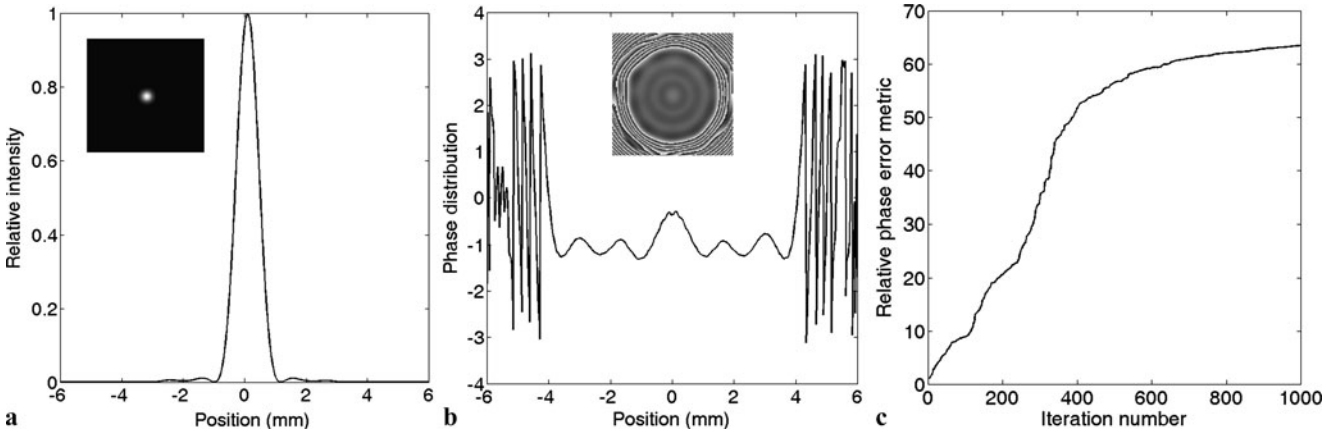

Fig. 6 Intensity and phase distribution of the beam (with no wavefront distortion) after passing through the adaptive compensation system: (**a**) far-field intensity distribution, (**b**) phase distribution, (**c**) evolution of the relative phase error metric during SPGD algorithm execution

is shown in the following paragraphs. The SPGD algorithm is used to optimize the quality metric and the steps can be briefly described as follows [24]:

1. Generate statistically independent random perturbations $\delta a_2, \ldots, \delta a_n$, where all δa_i are small values that are typically chosen as statistically independent variables having zero mean and equal variances, $\langle \delta a_i \rangle = 0$, $\langle \delta a_i \delta a_i \rangle = \sigma^2 \delta_{ij}$, where δ_{ij} is the Kronecker symbol.
2. Apply the control signal with perturbations and get the metric function from the CCD camera, $J_+ = J(a_2 + \delta a_2, \ldots, a_n + \delta a_n)$, then apply the control signals with the opposite perturbations and get the metric function, $J_- = J(a_2 - \delta a_2, \ldots, a_n - \delta a_n)$. Calculate the difference $\delta J = J_+ - J_-$.
3. Update the control signals, $a_i = a_i + \gamma \delta a_i \delta J, i = 2, \ldots, n$, where γ is the update gain: $\gamma > 0$ and $\gamma < 0$ according to the procedure of maximization and minimization, respectively.

The phase error metric is chosen as the metric function and is given by

$$J_{\text{Compensation}} = \iint I_{\text{farfield}}(x, y)^2 \, dx \, dy, \tag{10}$$

where $I_{\text{farfield}}(x, y)$ is the intensity distribution of the focal spot of the output beam. According to the analysis of Vorontsov, the global maximum of $J_{\text{Compensation}}$ corresponds to an undistorted wavefront [23]. In simulation, the lens with focal length 5.5 m is used to focus the output beam. The SPGD algorithm is performed with Zernike polynomials $\{Z_i(r, \theta)\}$ $(i = 2, \ldots, 120)$ as a set of influence functions. During the process, the algorithm adaptively optimizes the phase distribution of the output beam to realize the undistorted wavefront. Figure 6(a), (b) and (c), shows the results of the beam (with no wavefront distortion, corresponding to Fig. 3) after passing through the adaptive compensation system. It can be found that after 900 iterations, the relative phase error metric approximately approaches an absolute maximum value. The far-field intensity distribution exhibits airy disk pattern.

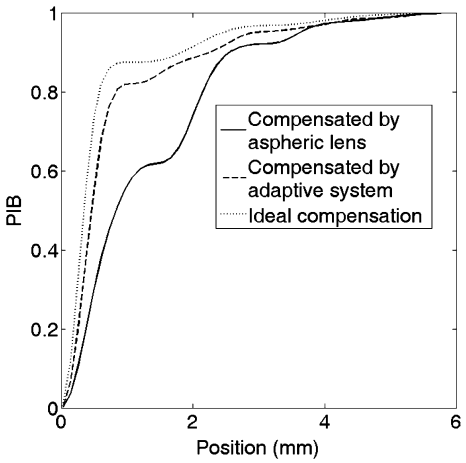

Fig. 7 Power in the bucket curves of the ideal compensated output beam, output beam compensated by the second aspheric lens and the adaptive system

Based on Figs. 3(a) and 6(a), we calculate the power in the bucket (PIB) curves of the far-field intensity distribution of the output beam compensated by the second aspheric lens and compensated by the adaptive system based on SPGD algorithm. The results are shown in Fig. 7. The power in the bucket is defined as

$$\text{PIB} = \frac{\int_0^b I_{\text{farfield}}(r) r \, dx}{\int_0^{+\infty} I_{\text{farfield}}(r) r \, dx}, \tag{11}$$

where $I_{\text{farfield}}(r)$ is the far-field intensity (focal spot) distribution of the output beam, b is the radius of the bucket. In the far field, the power in the main lobe of the airy disk pattern area of the output beam compensated by the adaptive

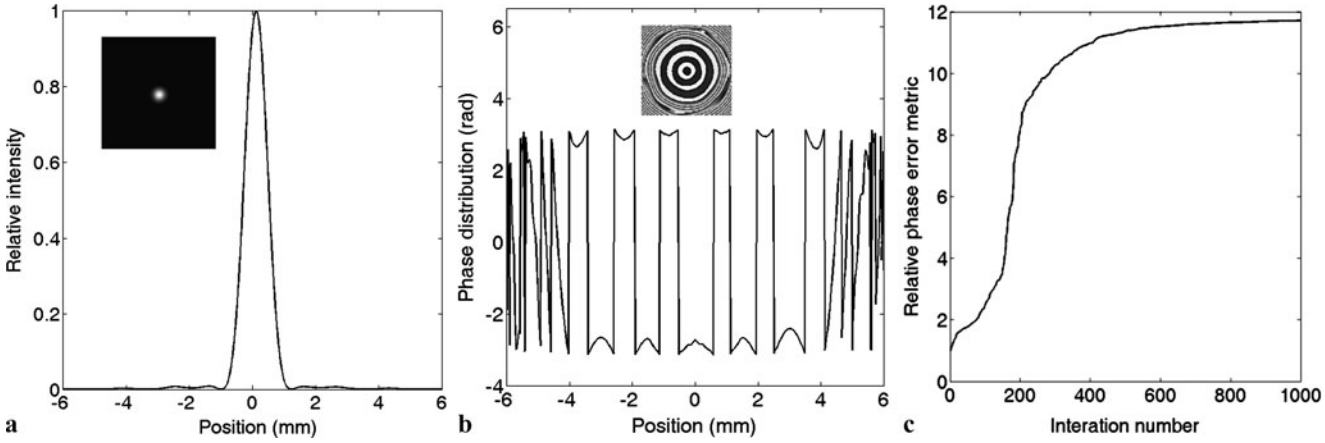

Fig. 8 Intensity and phase distributions of the beam with defocus aberration ($f = 6$ m) passing through the adaptive compensation system: (**a**) far-field intensity distribution, (**b**) phase distribution, (**c**) evolution of the relative phase error metric during the SPGD algorithm execution

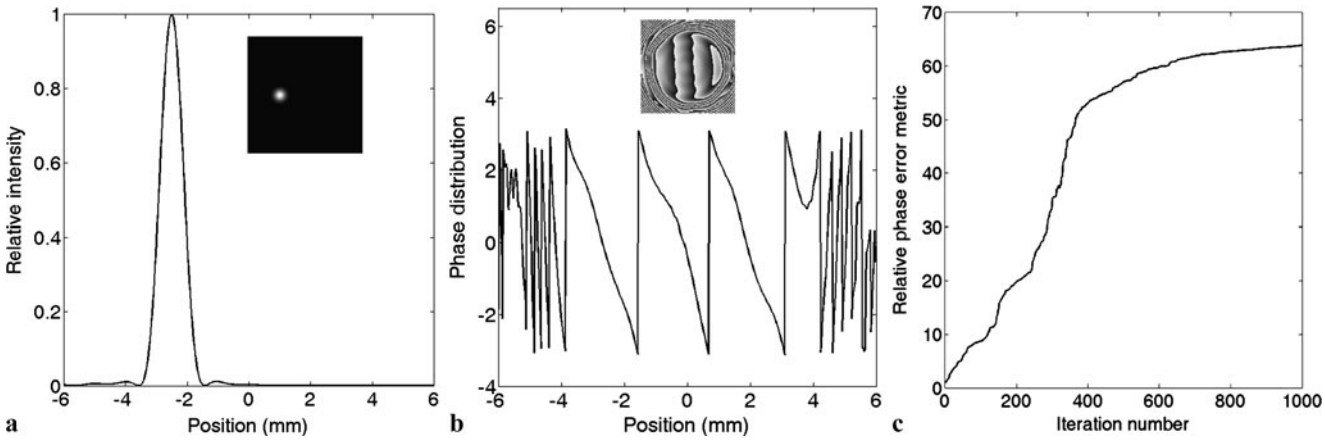

Fig. 9 Intensity and phase distribution of the beam with tilt aberration ($t_x = 0.5$ mrad) passing through the adaptive compensation system: (**a**) far-field intensity distribution, (**b**) phase distribution, (**c**) evolution of the relative phase error metric during the SPGD algorithm execution

system is 1.3 times larger than that compensated by the second aspheric lens in the conventional refractive beam shaping system.

Figure 8(a), (b) and (c), shows the beam with defocus aberration ($f = 6$ m, corresponding to Fig. 4) passing through the adaptive wavefront compensation system. It can be found that the relative phase error metric approaches an approximately maximum value after 700 iterations (the nearly plane wavefront is realized). Figure 9(a), (b) and (c), shows the beam with tilt aberration ($t_x = 0.5$ mrad, corresponding to Fig. 5) passing through the adaptive wavefront compensation system. It can be found that the relative phase error metric approaches an approximately maximum value after 800 iterations. The far-field intensity distribution exhibits airy disk pattern.

From Figs. 6–9, it can be found that the output beam (with phase aberration or without phase aberration) can be effectively compensated by the adaptive system with SPGD algorithm. The energy concentration of the far-field intensity distribution of the output beam compensated by the adaptive system is larger than that compensated by the second aspheric lens.

3 Experimental analysis

We apply the technique to the problem of transformation of a quasi-Gaussian beam into a near-diffraction-limited dark hollow beam. The experimental setup is shown schematically in Fig. 10. The essential instruments are the parallel aligned nematic LC-SLMs from BNS company (LC-SLM1 with $512\times51215\times15$ μm^2 pixels, LC-SLM2 with $256\times25624\times24$ μm^2 pixels), which are phase only modulator. The polarizer is oriented parallel to the LC director. The Nd:YVO_4 laser with 1064 nm wavelength is expanded and collimated by a telescope. Reflected by LC-SLM1, the beam is separated into two parts: the main beam is incident on LC-SLM2 and the other is incident on CCD1. The beam reflected by LC-SLM2 is also divided into two parts. One is focused on the detection surface of CCD2 by a plano-convex

lens with 67 cm focal length. CCD1 (Dolphin F-145B, 15 Hz) with $1392 \times 10406.45 \times 6.45\ \mu m^2$ pixels and CCD2 (Guppy F080B, 30 Hz) with $1032 \times 7784.65 \times 4.65\ \mu m^2$ pixels are used to diagnose the near-field and far-field intensity distribution of the output beam. The CCD camera is directly interfaced using IEEE 1394 (Firewire) connections and is addressed under VC++ control by using SPGD program, which also controls LC-SLM2. By monitoring and processing images from CCD2, the system is capable of adjusting phase distributions of LC-SLM2 adaptively to compensate the wavefront of the output beam.

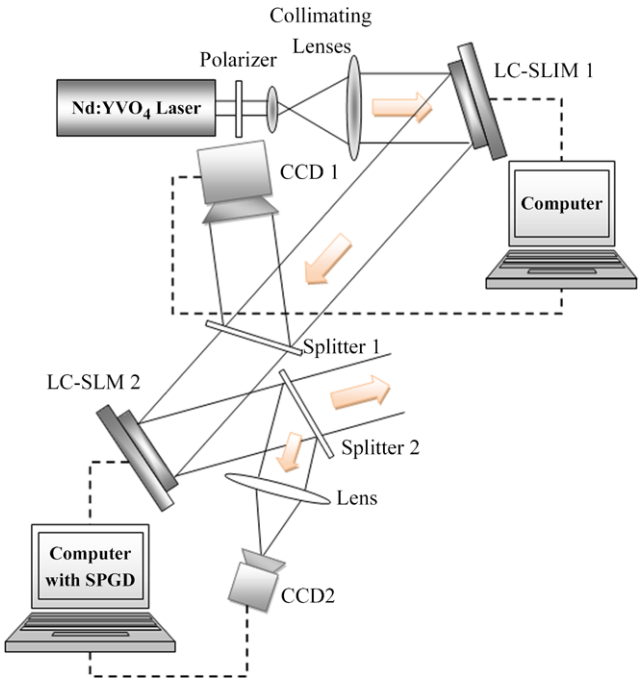

Fig. 10 Experimental setup for generation of near-diffraction-limited dark hollow beam

In the experiment, LC-SLM1 redistributes the intensity based on the refractive beam shaping system and LC-SLM2 adaptively compensates the wavefront of the output beam based on SPGD algorithm. To ensure the intensity distribution recorded by CCD1 is the same as the one incident on LC-SLM2, the optical length between CCD1 and LC-SLM1 is the same as the optical length between LC-SLM2 and LC-SLM1. In this paper, the optical length is about 40 cm. The intensity distribution of the input beam is shown in Fig. 11(a). It can be found that the intensity distribution is not the ideal Gaussian profile. We use the Gaussian profile combination to expand the input beam, which is shown in (12).

$$P_{\text{input}}(r) = \sum_i e_i \exp\left(\frac{-2r^2}{w_i^2}\right), \tag{12}$$

where w_i and e_i are the beam waist and coefficient of the Gaussian beam. The result of Gaussian profile combination expansion is shown in Fig. 11(a). The hollow Gaussian beam with parameters $w = 0.85$ mm, and $p = 3$ is chosen as the target profile. Based on the refractive beam shaping system, we calculate the surface and phase distribution of the first aspheric lens. By loading the phase distribution onto LC-SLM1, the dark hollow beam in the near field can be realized and is shown in Fig. 11(b). It is recognized that there exist errors between the output beam shape and target shape, which are mainly introduced by the CCD noise and departure of Gaussian profile combination from the real intensity distribution of the input beam. The corresponding far-field intensity distribution (focused by a lens with focal length 67 cm) is shown in Fig. 11(c). Because of the phase aberration introduced by intensity redistribution and other optical elements, the far-field energy concentration is low.

According to the analysis mentioned in the second section, the far-field intensity distribution of the output beam

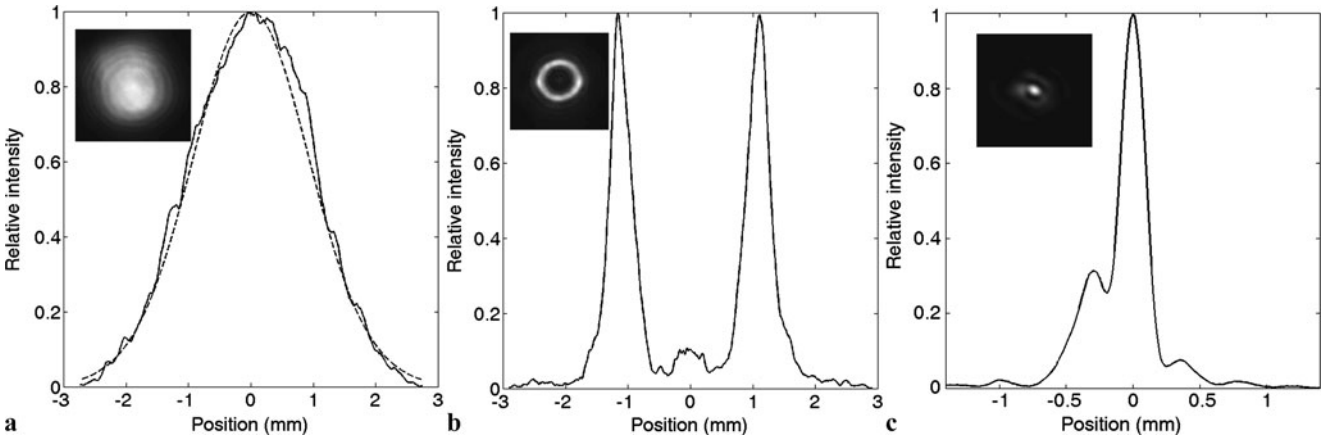

Fig. 11 Intensity distributions of the input and output beam: (**a**) intensity distribution of the input beam, (**b**) intensity distribution of the output beam, (**c**) corresponding far-field intensity distribution without being compensated by the LC-SLM2

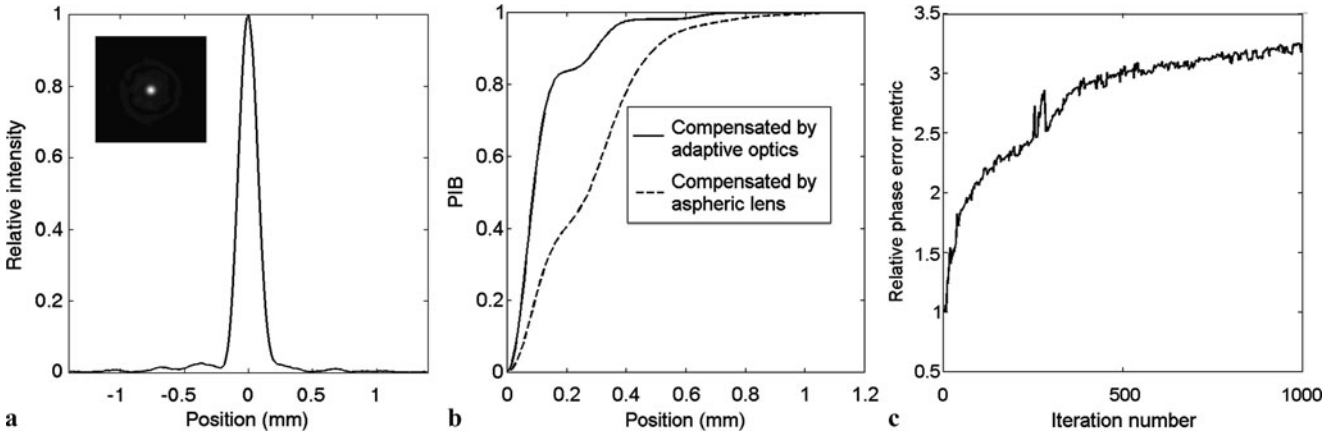

Fig. 12 Experimental results for adaptive compensation of the output beam: (**a**) far-field intensity distribution of the output beam, (**b**) power in the bucket curves before and after adaptive compensation, (**c**) evolution of the relative phase error metric during the SPGD algorithm execution

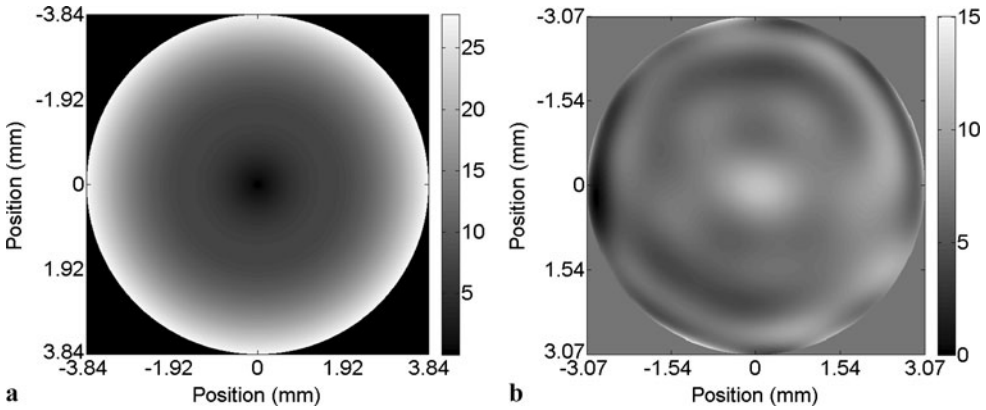

Fig. 13 Phase distributions generated by the hybrid control way: (**a**) phase distribution for LC-SLM1 generated based on the refractive beam shaping system, (**b**) phase distribution for LC-SLM2 generated based on adaptive optics by using SPGD algorithm

compensated by the adaptive compensation system based on the SPGD algorithm is larger than that compensated by the second aspheric lens based on the refractive beam shaping system. In closed control loop of the wavefront compensation, the SPGD algorithm is performed for a modal wavefront corrector with Zernike polynomials $\{Z_i(r,\theta)\}$ $(i = 2,\ldots,80)$ as a set of influence functions. During the process, the SPGD algorithm adaptively optimizes the phase distribution of LC-SLM2 to compensate the wavefront of output beam. The results are shown in Fig. 12(a), (b) and (c).

As shown in Fig. 12(a), (b) and (c), it can be found that after 1000 iterations, the relative phase error metric approximately approaches an absolute maximum value. The far-field intensity distribution exhibits airy disk pattern, which indicates good wavefront flatness. The phase distributions for LC-SLM1 and LC-SLM2 generated by the hybrid control way in the experiment are shown in Fig. 13(a) and (b).

4 Conclusion

The conversion of quasi-Gaussian beam into dark hollow beam with plane wavefront in the near field based on the hybrid control way by using dual phase only LC-SLMs has been experimentally demonstrated. The intensity redistribution is based on the working principle of refractive beam shaping system and the wavefront compensation is based on adaptive optics by using SPGD algorithm. The shaping effect and influences of phase distortion on laser beam shaping are analyzed in detail. The numerical simulation and experimental results show that the conversion of quasi-Gaussian beam with or without small wavefront distortion into near-diffraction-limited dark hollow beam can be realized easily by using the hybrid control way. Compared with the conventional refractive beam shaping system, the hybrid control way can not only improve the far-field energy concentration of the output beam (the power in the main lobe of the airy disk pattern area in the far field is about 1.3 times larger than that generated by the refractive beam shaping system), but also can correct the dynamic phase distortion. The hybrid control way, which provides a convenient and powerful way to translate central symmetric intensity distribution to central symmetric intensity distributions, can not only be used for controlling dual phase only LC-SLMs or high spatial resolution DMs for near-field beam shaping, but also be used for generating phase distributions for diffractive and refractive beam shaping systems.

References

1. Y. Baykal, J. Opt. Soc. Am. A **22**, 672 (2005)
2. H.T. Eyyuboglu, Y. Baykal, J. Opt. Soc. Am. A **24**, 156 (2007)
3. X. Chu, G. Zhou, Opt. Express **15**, 7697 (2007)
4. P.G. Hannan, Appl. Opt. **31**, 513 (1992)
5. Y. Cai, S. He, Opt. Express **14**, 1353 (2006)
6. Y. Yuan, Y. Cai, J.Q.H.T. Eyyuboğlu, Y. Baykal, O. Korotkova, Opt. Express **17**, 17344 (2009)
7. W.L. Power, L. Allen, M. Babiker, V.E. Lembessis, Phys. Rev. A **52**, 479 (1995)
8. C. Zhao, Y. Cai, F. Wang, X. Lu, Y. Wang, Opt. Lett. **33**, 1380 (2008)
9. A. Jesacher, C. Maurer, A. Schwaighofer, S. Bernet, M. Ritsch-Marte, Opt. Express **16**, 4479 (2008)
10. H.S. Lee, B.W. Stewart, K. Choi, H. Fenichel, Phys. Rev. A **49**, 4922 (1994)
11. X. Wang, M.G. Littman, Opt. Lett. **18**, 767 (1993)
12. J. Yin, H. Noh, K. Lee, K. Kim, Y. Wang, W. Jhe, Opt. Commun. **138**, 287 (1997)
13. A.V. Mamaev, M. Saffman, A.A. Zozulya, Phys. Rev. Lett. **77**, 4544 (1996)
14. V. Tikhonenko, N.N. Akhmediev, Opt. Commun. **126**, 108 (1996)
15. Y. Xia, J.P. Yin, J. Opt. Soc. Am. B **22**, 529 (2005)
16. J.A. Hoffnagle, C.M. Jefferson, Appl. Opt. **39**, 5488 (2000)
17. C. Liu, S. Zhang, Opt. Express **16**, 6675 (2008)
18. J.L. Kreuzer, U.S. Patent 3,476,463 (1969)
19. J. Liang, R.N. Kohn Jr., M.F. Becker, D.J. Heinzen, Appl. Opt. **48**, 2009 (1955)
20. H. Ma, P. Zhou, X. Wang, Y. Ma, F. Xi, X. Xu, Z. Liu, Opt. Express **18**, 8251 (2010)
21. R. El-Agmy, H. Bulte, A.H. Greenaway, D. Reid, Opt. Express **13**, 6085 (2005)
22. E.J. Fernández, P.M. Prieto, P. Artal, Opt. Express **17**, 11013 (2009)
23. M.A. Vorontsov, V.P. Sivokon, J. Opt. Soc. Am. A **15**, 2745 (1998)
24. P. Zhou, Y. Ma, X. Wang, H. Ma, X. Xu, Z. Liu, Opt. Lett. **34**, 2939 (2009)